

Numerical modeling of ground-penetrating radar in 2-D using MATLAB[☆]

James Irving*, Rosemary Knight

Geophysics Department, Stanford University, Room 360, Mitchell Building, Stanford, CA 94305, USA

Received 29 August 2005; received in revised form 13 November 2005; accepted 14 November 2005

Abstract

We present MATLAB codes for finite-difference time-domain (FDTD) modeling of ground-penetrating radar (GPR) in two dimensions. Surface-based reflection GPR is modeled using a transverse magnetic (TM-) mode formulation. Crosshole and vertical radar profiling (VRP) geometries are modeled using a transverse electric (TE-) mode formulation. Matrix notation is used in the codes wherever possible to optimize them for speed in the MATLAB environment. To absorb waves at the edges of the modeling grid, we implement perfectly matched layer (PML) absorbing boundaries. Although our codes are two-dimensional and do not incorporate features such as dispersion in electrical properties, they capture many of the important elements of GPR surveying and run at a fraction of the computational cost of more elaborate algorithms. In addition, the codes are well commented, relatively easy to understand, and can be easily modified for the user's specific purpose.

© 2005 Elsevier Ltd. All rights reserved.

Keywords: Ground-penetrating radar; GPR; Numerical modeling; Electromagnetics; Finite-difference time domain; FDTD

1. Introduction

Ground-penetrating radar (GPR) is a popular geophysical method for high-resolution imaging of the shallow subsurface. The GPR technique can be divided into two main modes of operation: (i) surface-based reflection surveying, where the transmitter and receiver antennas are located on the surface of the earth and the subsurface is imaged in terms of changes in its electrical properties, and

(ii) borehole surveying, where one or both antennas are located in boreholes and subsurface properties are estimated tomographically. Of interest in our research is the application of both surface and borehole GPR to hydrogeological problems. Specifically, we are interested in using these techniques to assist in the development of hydrogeological models that predict groundwater flow and contaminant transport. A critical step in using GPR for this purpose is determining the link between the hydrogeological properties that govern these processes, and the information contained in a GPR data set.

Numerical GPR models provide one means of exploring the link between subsurface properties and GPR data. We can create a model of a subsurface region of interest, where we define the

[☆] Code available from server at <http://www.iamg.org/CGEditor/index.htm>

*Corresponding author. Tel.: +1 650 724 9939;
fax: +1 650 725 7344.

E-mail addresses: jdirving@pangea.stanford.edu (J. Irving),
rknight@pangea.stanford.edu (R. Knight).

subsurface in terms of its lithological or hydrogeological properties. We can then transform this model into one that represents the subsurface in terms of its electrical properties. GPR modeling can then be used to simulate the acquisition of data in this subsurface region. The synthetic data that are obtained can be used to advance our understanding of the way in which information about the spatial variability of subsurface properties is captured by, and can be extracted from, GPR data.

A number of approaches have been presented for the numerical modeling of GPR data. These include ray-based methods (Goodman, 1994; Cai and McMechan, 1995), frequency-domain methods (Powers and Olhoeft, 1994; Zeng et al., 1995), integral methods (Ellefson, 1999), and pseudospectral methods (Carcione, 1996; Casper and Kung, 1996; Lui and Fan, 1999). What has become by far the most common approach for GPR modeling over the past decade, however, is the finite-difference time-domain (FDTD) technique (e.g., Wang and Tripp, 1996; Bourgeois and Smith, 1996; Bergmann et al., 1996; Teixeira et al., 1998; Holliger and Bergman, 2002). Reasons for this include that the FDTD approach is relatively conceptually simple, accurate for arbitrarily complex models, and capable of accommodating realistic antenna designs and features such as dispersion in electrical properties (Taflove, 1995). What is lacking, however, are FDTD modeling codes for GPR, freely available for the public use, that are easy to understand and modify.

Here, we present FDTD codes, written in the MATLAB programming language, for basic surface reflection and borehole GPR modeling in two dimensions. Although 2-D modeling is limited in the sense that it cannot fully account for antenna behavior and out-of-plane variations in material properties, our codes capture many of the important features of GPR surveying and run at a fraction of the computational cost of fully 3-D algorithms. The codes feature perfectly matched layer (PML) absorbing boundaries to avoid reflections from the edges of the modeling grid. To optimize the programs for speed in MATLAB, matrix notation is used wherever possible. To begin, we discuss the theory behind our codes, including the governing analytical equations, their finite-difference approximations, numerical stability and dispersion criteria, and boundary conditions. Next, we briefly discuss how the FDTD equations are implemented in the MATLAB environment. Finally, we present two

examples of the use of our codes, one showing modeling of a reflection GPR survey and the other modeling of a crosshole GPR survey.

2. Theory

2.1. Governing equations

We begin the theory behind our GPR modeling codes with Maxwell's curl equations in the frequency domain, which are

$$\nabla \times \mathbf{E} = -i\omega\mu\mathbf{H}, \quad (1)$$

$$\nabla \times \mathbf{H} = \sigma\mathbf{E} + i\omega\epsilon\mathbf{E}, \quad (2)$$

where $i = \sqrt{-1}$, ω is angular frequency, ϵ , μ , and σ are the dielectric permittivity, magnetic permeability, and electrical conductivity parameters, respectively, and \mathbf{E} and \mathbf{H} are the electric and magnetic field vectors. To implement PML absorbing boundaries in our codes, we consider the general case of a complex stretched coordinate space (e.g., Chew and Weedon, 1994; Gedney, 1998), where the ∇ operator takes the following form:

$$\nabla = \hat{x} \frac{1}{s_x} \frac{\partial}{\partial x} + \hat{y} \frac{1}{s_y} \frac{\partial}{\partial y} + \hat{z} \frac{1}{s_z} \frac{\partial}{\partial z}, \quad (3)$$

where

$$s_k = \kappa_k + \frac{\sigma_k}{\alpha_k + i\omega\epsilon_0}, \quad k = x, y, z \quad (4)$$

are complex coordinate stretching variables that vary only in the k direction (Kuzuoglu and Mittra, 1996). Here, ϵ_0 is the dielectric permittivity of free space, and σ_k , κ_k , and α_k are parameters that can be specified to allow for wave propagation in the interior of the modeling grid and wave absorption in the PML boundary regions. It should be stressed that σ_k , κ_k , and α_k are not true electrical properties. Rather they are parameters that, through complex coordinate stretching, add additional degrees of freedom to Maxwell's equations to allow for PML boundary implementation.

Taking the components of Eqs. (1) and (2) using the identity in Eq. (3), and assuming that there is no variation in the y direction for 2-D modeling, we arrive at the following two decoupled sets of partial-differential equations involving the $\{H_x, H_z, E_y\}$ and $\{E_x, E_z, H_y\}$ field components:

$$i\omega\mu H_x = -\frac{1}{s_z} \frac{\partial E_y}{\partial z}, \quad (5a)$$

$$i\omega\mu H_z = \frac{1}{s_x} \frac{\partial E_y}{\partial x}, \quad (5b)$$

$$\sigma E_y + i\omega\varepsilon E_y = \frac{1}{s_x} \frac{\partial H_z}{\partial x} - \frac{1}{s_z} \frac{\partial H_x}{\partial z} \quad (5c)$$

and

$$\sigma E_x + i\omega\varepsilon E_x = \frac{1}{s_z} \frac{\partial H_y}{\partial z}, \quad (6a)$$

$$\sigma E_z + i\omega\varepsilon E_z = -\frac{1}{s_x} \frac{\partial H_y}{\partial x}, \quad (6b)$$

$$i\omega\mu H_y = \frac{1}{s_z} \frac{\partial E_x}{\partial z} - \frac{1}{s_x} \frac{\partial E_z}{\partial x}. \quad (6c)$$

Eqs. (5a)–(5c) and (6a)–(6c) are the transverse magnetic (TM-) and transverse electric (TE-) mode sets of equations in the stretched coordinate space, respectively. For surface-based reflection GPR modeling, where the antennas are oriented perpendicular to the x – z survey plane, we use the TM-mode equations. For crosshole and vertical radar profiling (VRP) geometries, where the antennas are contained within the survey plane, the TE-mode equations are employed. It is important to note that when the stretching parameters are set to unity, Eqs. (5a)–(5c) and (6a)–(6c) become the standard TM- and TE-mode equations in an unstretched coordinate space. In the interior of the modeling grid, we therefore set $s_x = s_z = 1$. In the PML boundary regions of the grid, however, s_x and s_z are given complex values, which allows significant wave absorption to occur. Unlike in the simpler case of a change in electrical conductivity in these regions (which would also cause absorption), altering the coordinate stretching variables does not result in a change in electromagnetic (EM) impedance from the interior of the grid, and thus no reflections are created at the edges of the PML domain.

We implement PML absorbing boundaries in our modeling codes using the convolutional PML (CPML) approach of Roden and Gedney (2000). This method makes use of time-domain expressions for $1/s_x$ and $1/s_z$ in the FDTD formulation, and avoids the splitting of the electric and magnetic field components common in other PML approaches (e.g., Berenger, 1994; Fang and Wu, 1996). For this reason, we find the CPML approach to be the most intuitive implementation of PML. Taking the inverse Fourier transform of the inverse of Eq. (4),

we have

$$\begin{aligned} s_k^{-1}(t) &= \frac{\delta(t)}{\kappa_k} - \frac{\sigma_k}{\varepsilon_0 \kappa_k^2} \exp\left[-\frac{t}{\varepsilon_0} \left(\frac{\sigma_k}{\kappa_k} + \alpha_k\right)\right] u(t) \\ &= \frac{\delta(t)}{\kappa_k} + \zeta_k(t), \end{aligned} \quad (7)$$

where $\delta(t)$ is the Dirac delta function and $u(t)$ is the Heaviside step function. Using this expression and assuming frequency-independent material properties, Eqs. (5a)–(5c) and (6a)–(6c) are transformed into the time domain as follows:

$$\mu \frac{\partial H_x}{\partial t} = -\frac{1}{\kappa_z} \frac{\partial E_y}{\partial z} - \zeta_z(t) * \frac{\partial E_y}{\partial z}, \quad (8a)$$

$$\mu \frac{\partial H_z}{\partial t} = \frac{1}{\kappa_x} \frac{\partial E_y}{\partial x} + \zeta_x(t) * \frac{\partial E_y}{\partial x}, \quad (8b)$$

$$\begin{aligned} \sigma E_y + \varepsilon \frac{\partial E_y}{\partial t} &= \frac{1}{\kappa_x} \frac{\partial H_z}{\partial x} - \frac{1}{\kappa_z} \frac{\partial H_x}{\partial z} \\ &\quad + \zeta_x(t) * \frac{\partial H_z}{\partial x} - \zeta_z(t) * \frac{\partial H_x}{\partial z} \end{aligned} \quad (8c)$$

and

$$\sigma E_x + \varepsilon \frac{\partial E_x}{\partial t} = \frac{1}{\kappa_z} \frac{\partial H_y}{\partial z} + \zeta_z(t) * \frac{\partial H_y}{\partial z}, \quad (9a)$$

$$\sigma E_z + \varepsilon \frac{\partial E_z}{\partial t} = -\frac{1}{\kappa_x} \frac{\partial H_y}{\partial x} - \zeta_x(t) * \frac{\partial H_y}{\partial x}, \quad (9b)$$

$$\mu \frac{\partial H_y}{\partial t} = \frac{1}{\kappa_z} \frac{\partial E_x}{\partial z} - \frac{1}{\kappa_x} \frac{\partial E_z}{\partial x} + \zeta_z(t) * \frac{\partial E_x}{\partial z} - \zeta_x(t) * \frac{\partial E_z}{\partial x}, \quad (9c)$$

where $*$ represents convolution. We now describe how Eqs. (8a)–(8c) are approximated using finite-differences in our TM-mode modeling code for GPR reflection profiling. The derivations for the TE-mode modeling code using Eqs. (9a)–(9c) are not included here, as they are performed in a nearly identical manner.

2.2. Finite-difference approximations

To numerically model Eqs. (8a)–(8c), we use a leap-frog, staggered-grid approach that involves offsetting the electric and magnetic field components in both space and time such that the finite-difference approximations of the partial derivatives in each equation are centered on the same spatio-temporal location (Yee, 1966). Fig. 1 shows the configuration of H_x , H_z , and E_y in space for our TM-mode modeling code. All spatial derivatives are

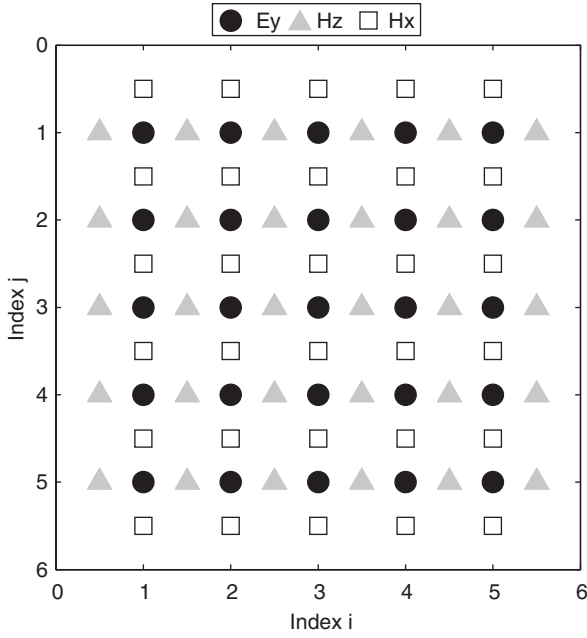


Fig. 1. Spatial arrangement of H_x , H_z , and E_y field components for TM-mode modeling. Electric and magnetic field components are also staggered in time by $\Delta t/2$.

approximated using fourth-order-accurate finite-difference expressions. The time derivatives are approximated with second-order-accurate expressions. This $O(2,4)$ scheme is identical to that described in Bergmann et al. (1996) for 1-D GPR modeling. The conduction current density term in Eq. (8c) is modeled using a semi-implicit approximation (e.g., Taflov, 1995, p. 64) which has been shown to have superior numerical properties over one-sided expressions for this term (Bergmann et al., 1996).

After substituting the appropriate finite-difference expressions into Eqs. (8a)–(8c) and solving for the updated electric and magnetic field components, we arrive at the following FDTD update equations:

$$H_x|_{i,j+1/2}^{n+1/2} = H_x|_{i,j+1/2}^{n-1/2} - D_{b_z}|_{i,j+1/2} \left[-E_y|_{i,j+2}^n + 27E_y|_{i,j+1}^n - 27E_y|_{i,j}^n + E_y|_{i,j-1}^n \right] - D_c|_{i,j+1/2} \left[\Psi_{H_{xz}}|_{i,j+1/2}^n \right], \quad (10a)$$

$$H_z|_{i+1/2,j}^{n+1/2} = H_z|_{i+1/2,j}^{n-1/2} + D_{b_x}|_{i+1/2,j} \left[-E_y|_{i+2,j}^n + 27E_y|_{i+1,j}^n - 27E_y|_{i,j}^n + E_y|_{i-1,j}^n \right] + D_c|_{i+1/2,j} \left[\Psi_{H_{zx}}|_{i+1/2,j}^n \right], \quad (10b)$$

$$E_y|_{i,j}^{n+1} = C_a|_{i,j} [E_y|_{i,j}^n] + C_{b_x}|_{i,j} \left[-H_z|_{i+3/2,j}^{n+1/2} + 27H_z|_{i+1/2,j}^{n+1/2} - 27H_z|_{i-1/2,j}^{n+1/2} + H_z|_{i-3/2,j}^{n+1/2} \right] - C_{b_z}|_{i,j} \left[-H_x|_{i,j+3/2}^{n+1/2} + 27H_x|_{i,j+1/2}^{n+1/2} - 27H_x|_{i,j-1/2}^{n+1/2} + H_x|_{i,j-3/2}^{n+1/2} \right] + C_c|_{i,j} \left[\Psi_{E_{yx}}|_{i,j}^{n+1/2} - \Psi_{E_{yz}}|_{i,j}^{n+1/2} \right], \quad (10c)$$

where the subscripts indicate spatial position and the superscripts indicate time (i.e., $H_x|_{i,j+1/2}^{n+1/2}$ represents the H_x field component at position $(x, z) = (i\Delta x, (j+1/2)\Delta z)$ and time $t = (n+1/2)\Delta t$, where Δx and Δz are the horizontal and vertical field discretization intervals, and Δt is the time step). FDTD modeling using these equations is accomplished by alternately updating the electric and magnetic fields. This moves forward in time since the two fields are temporally staggered by $\Delta t/2$. As can be seen from the equations, all field updates are fully explicit.

The update coefficients C_a , C_{b_x} , C_{b_z} , C_c , D_{b_x} , D_{b_z} , and D_c in Eqs. (10a)–(10c) are given in terms of the electrical properties and grid parameters as follows:

$$C_a = \left(1 - \frac{\sigma \Delta t}{2\varepsilon} \right) \left(1 + \frac{\sigma \Delta t}{2\varepsilon} \right)^{-1}, \quad (11a)$$

$$C_{b_k} = \frac{\Delta t}{\varepsilon} \left(1 + \frac{\sigma \Delta t}{2\varepsilon} \right)^{-1} (24\kappa_k \Delta k)^{-1}, \quad (11b)$$

$$C_c = \frac{\Delta t}{\varepsilon} \left(1 + \frac{\sigma \Delta t}{2\varepsilon} \right)^{-1}, \quad (11c)$$

$$D_{b_k} = \frac{\Delta t}{\mu} (24\kappa_k \Delta k)^{-1}, \quad (11d)$$

$$D_c = \frac{\Delta t}{\mu}. \quad (11e)$$

Although not explicitly indicated, these coefficients are all functions of position since ε , μ , σ , κ_x , and κ_z are, in general, spatially varying. The convolution terms in Eqs. (8a)–(8c) are modeled using the recursive convolution technique (Luebbers and Hunsberger, 1992), and are accounted for in Eqs. (10a)–(10c) through the $\Psi_{H_{xz}}$, $\Psi_{H_{zx}}$, $\Psi_{E_{yx}}$, and $\Psi_{E_{yz}}$ terms. These are defined as

$$\Psi_{H_{xz}}|_{i,j+1/2}^n = B_z|_{i,j+1/2} \left[\Psi_{H_{xz}}|_{i,j+1/2}^{n-1} + A_z|_{i,j+1/2} \left[-E_y|_{i,j+2}^n + 27E_y|_{i,j+1}^n - 27E_y|_{i,j}^n + E_y|_{i,j-1}^n \right] \right], \quad (12a)$$

$$\begin{aligned}\Psi_{H_{xz}}|_{i+1/2,j}^n &= B_x|_{i+1/2,j} \left[\Psi_{H_{xz}}|_{i+1/2,j}^{n-1/2} \right] \\ &+ A_x|_{i+1/2,j} \left[-E_y|_{i+2,j}^n + 27E_y|_{i+1,j}^n \right. \\ &\left. - 27E_y|_{i,j}^n + E_y|_{i-1,j}^n \right],\end{aligned}\quad (12b)$$

$$\begin{aligned}\Psi_{E_{yx}}|_{i,j}^{n+1/2} &= B_x|_{i,j} \left[\Psi_{E_{yx}}|_{i,j}^{n-1/2} \right] \\ &+ A_x|_{i,j} \left[-H_z|_{i+3/2,j}^{n+1/2} + 27H_z|_{i+1/2,j}^{n+1/2} \right. \\ &\left. - 27H_z|_{i-1/2,j}^{n+1/2} + H_z|_{i-3/2,j}^{n+1/2} \right],\end{aligned}\quad (12c)$$

$$\begin{aligned}\Psi_{E_{yz}}|_{i,j}^{n+1/2} &= B_z|_{i,j} \left[\Psi_{E_{yz}}|_{i,j}^{n-1/2} \right] \\ &+ A_z|_{i,j} \left[-H_x|_{i,j+3/2}^{n+1/2} + 27H_x|_{i,j+1/2}^{n+1/2} \right. \\ &\left. - 27H_x|_{i,j-1/2}^{n+1/2} + H_x|_{i,j-3/2}^{n+1/2} \right],\end{aligned}\quad (12d)$$

where

$$A_k = \frac{\sigma_k}{\sigma_k \kappa_k + \alpha_k \kappa_k^2} (B_k - 1), \quad (13a)$$

$$B_k = \exp \left[-\frac{\Delta t}{\varepsilon_0} \left(\frac{\sigma_k}{\kappa_k} + \alpha_k \right) \right] \quad (13b)$$

are PML update coefficients that, again, vary with location in the modeling grid. As can be seen from Eqs. (12a)–(12d), the values of the convolution terms at the current time step are computed from those at the previous time step. Therefore $\Psi_{H_{xz}}$, $\Psi_{H_{yz}}$, $\Psi_{E_{yx}}$, and $\Psi_{E_{yz}}$ must be stored, in addition to the H_x , H_z , and E_y field components, during the FDTD simulation. Throughout the above equations, we have kept our notation consistent with that of Roden and Gedney (2000) so that their paper can be consulted for further details on CPML implementation.

To introduce an electric field source into the grid during FDTD modeling using Eqs. (10)–(13), we add a source pulse function to the update for the E_y field component at the desired spatial location. This amounts to adding the source function to the y -component of the current density term in Maxwell's equations. To model receivers in our code, we simply record the E_y field component as a function of time at the receiver locations. It must be stressed that, because our modeling codes are 2-D, all such sources and receivers are actually line elements, extending to positive and negative infinity in the dimension perpendicular to the survey plane. As a result, the radiation patterns and geometrical spreading for realistic, dipole-type GPR antennas cannot be properly modeled with our codes; this would require either a fully or pseudo 3-D approach

(e.g., Moghaddam et al., 1991; Xu and McMechan, 1997). Nevertheless, as stated previously, our 2-D codes capture many of the important features of reflection GPR surveying, and can provide much insight into the interaction of EM waves with a complex subsurface. They should be used with caution, however, when antenna radiation patterns play a critical role in how the data are analyzed. A key example is crosshole GPR attenuation tomography.

2.3. Numerical stability and dispersion criteria

An important step in FDTD modeling is choosing appropriate time and spatial discretization intervals for a simulation. Ideally, we would like to have Δx , Δz , and Δt as large as possible to make the simulation run most quickly. However, if Δt is too large, the FDTD scheme presented above will become numerically unstable. In addition, if Δx or Δz are too large, the electric and magnetic fields will be inadequately sampled in space and numerical dispersion will be the result. For the O(2,4) scheme presented here, the maximum time step that can be used, in order for the scheme to remain numerically stable, is (Georgakopoulos et al., 2002)

$$\Delta t_{\max} = \frac{6}{7} \sqrt{\frac{\mu_{\min} \varepsilon_{\min}}{(1/\Delta x^2 + 1/\Delta z^2)}}, \quad (14)$$

where μ_{\min} and ε_{\min} are the minimum magnetic permeability and dielectric permittivity values present in the modeling grid. To control numerical dispersion, the O(2,4) scheme must allow for five field samples per minimum wavelength (Bergmann et al., 1996; Georgakopoulos et al., 2002). The MATLAB programs `finddt.m` and `finddx.m` determine the maximum possible Δt , Δx , and Δz given a model's electrical properties as input, and should be run prior to starting any simulation.

2.4. PML absorbing boundaries

Compared with other absorbing boundary types, PML boundaries possess a number of significant advantages. First, the PML approach offers superior attenuation of reflections from the edges of the modeling grid, and requires only a small number of cells to be very effective (Gedney, 1998). Second, to implement PML, only the coordinate stretching variables need to be changed in the boundary regions, and not the FDTD update equations

(i.e., the same update equations are used everywhere in the grid). For this reason, PML is well suited to parallel implementations. Finally, the CPML approach that we have chosen for our codes has the advantage of being media independent (Roden and Gedney, 2000). That is, the approach is implemented in the same manner no matter what the properties of the materials being modeled. For example, our FDTD formulation could be modified to allow for dispersion in ϵ , μ , and σ (say, using the technique of Bergmann et al. (1998)), and the Ψ terms for invoking CPML in Eqs. (10a)–(10c) would remain unchanged.

As mentioned previously, in the interior of the modeling grid, the coordinate stretching variables, s_x and s_z , are set to unity such that Eqs. (10)–(13) become the standard, TM-mode, FDTD update equations in an unstretched coordinate space. This requires that $\kappa_x = \kappa_z = 1$ and $\sigma_x = \sigma_z = 0$ in these regions (see Eq. (4)). In the PML boundary regions, however, these parameters are given different values. Setting σ_x and σ_z greater than zero (which makes the stretching variables complex) allows propagating waves to be absorbed. Making κ_x and κ_z greater than one, on the other hand, allows the PML regions to absorb evanescent waves. Setting α_x and α_z greater than zero may also improve the absorption of evanescent modes (Kuzuoglu and Mittra, 1996; Roden and Gedney, 2000), although by default these parameters are set to zero in our codes.

In theory, because there is no change in electromagnetic impedance associated with a change in s_x and s_z , values for κ_x , κ_z , σ_x , and σ_z should be set as high as possible in the PML regions to achieve the most complete absorption of propagating and evanescent waves. In practice, however, in the discrete FDTD space, numerical reflections occur when electrical properties change too much between nodes. Consequently, the PML parameters must be set to gradually increase from their values in the interior of the grid to some maximum value at the grid edges. For κ_x and κ_z , we have

$$\kappa_k = \begin{cases} 1 & \text{in grid interior,} \\ 1 + \left(\frac{d}{\delta}\right)^m (\kappa_{k_{\max}} - 1) & \text{inside PML region,} \end{cases} \quad (15)$$

where d is the distance into the PML region from the interior/PML boundary, δ is the thickness of the PML region, m is known as the PML exponent, and

$\kappa_{k_{\max}}$ is the maximum value. Similarly, for σ_x and σ_z , we have

$$\sigma_k = \begin{cases} 0 & \text{in grid interior,} \\ \left(\frac{d}{\delta}\right)^m \sigma_{k_{\max}} & \text{inside PML region,} \end{cases} \quad (16)$$

where $\sigma_{k_{\max}}$ is the maximum value. Here, κ_k and σ_k vary only along the k direction since the coordinate stretching variables are one-dimensional functions. For example, σ_x will be zero throughout the interior of the modeling grid and non-zero only in the left and right PML regions. The κ_z parameter, on the other hand, will be one throughout the interior of the grid and greater than one only in the top and bottom PML regions. In our codes, we use $m = 4$ and set $\kappa_{x_{\max}} = \kappa_{z_{\max}} = 5$ by default, which we have found is adequate for the effective absorption of evanescent waves. The maximum value for σ_k is determined using the following criterion (Gedney, 1998):

$$\sigma_{k_{\max}} = \frac{m + 1}{150\pi\sqrt{\epsilon_r}\Delta k}, \quad (17)$$

where ϵ_r is the relative dielectric permittivity (i.e., the permittivity normalized to its value in free space) in the interior of the grid nearest to the PML boundary. In other words, in a heterogeneous medium, $\sigma_{k_{\max}}$ may vary depending on the permittivity values bounding the interior of the modeling domain. The natural boundaries in the grid interior are extended into the PML region by padding with PML cells before running a simulation (Chen and Chew, 1997).

3. MATLAB implementation

The 2-D, TM-mode, finite-difference formulation presented above has been implemented in the MATLAB environment in the code `TM_model2d.m`, for reflection GPR modeling. The MATLAB code for TE-mode modeling, suitable for crosshole and VRP surveys, is `TE_model2d.m`. To perform the FDTD simulations in MATLAB, we use matrices to store all field components and electrical properties. The property matrices are double the size of the field matrices because ϵ , μ , and σ are required at every electric and magnetic field component location (see Fig. 1). As inputs, `TM_model2d.m` and `TE_model2d.m` require the electrical property matrices, all source and receiver locations, a time vector and corresponding source

pulse sampled with the appropriate Δt , and the number of PML boundary cells to use. All finite-differences in the FDTD update equations are computed using matrix notation instead of loops to optimize the codes for speed in MATLAB. In addition, the FDTD and PML update coefficients are calculated and stored in matrices the same size as the electrical property matrices before starting a simulation, so that the number of calculations required during each iteration is reduced. Finally, the Ψ terms in Eqs. (10a)–(10c) are computed and added to the electric and magnetic fields only in the PML regions, as in the interior of the modeling grid, these terms become zero.

For the source pulse in our codes, we use the normalized first derivative of a Blackman–Harris window function (Harris, 1978), which is described in Chen and Chew (1997) for geophysical FDTD modeling. This pulse is created using the program `blackharrispulse.m`. Fig. 2 shows Blackman–Harris pulses having dominant frequencies of 50, 100, and 200 MHz. When fed into the E_y field component at the desired source location in our TM-mode code, the resulting pulse that travels through the grid and is recorded at the receiver locations roughly resembles a Ricker wavelet.

Fig. 3 is a flowchart showing the sequence of steps involved in simulating a reflection GPR survey with our TM-mode modeling code. First, the maximum spatial discretization intervals that can be used, in order to control numerical dispersion, are determined using `finddx.m` given the electrical properties in the model and the source pulse as inputs. Next, the code `finddt.m` is used to determine the

maximum time step that ensures numerical stability given the model's electrical properties, Δx , and Δz . If necessary, the electrical property matrices are interpolated to half the spatial discretization interval, since they are double the size of the field matrices, using the code `gridinterp.m`. As a final step before running a simulation, the property matrices are then padded around the edges with the proper number of PML absorbing boundary cells using the program `padgrid.m`. The values of σ , ϵ , and μ in the PML regions are set to be simply an extension of those in the interior of the grid.

In the code `TM_model2d.m`, an outer loop runs over the number of sources and an inner loop over the number of FDTD iterations required for each source. In each FDTD iteration, the H_x , H_z , and E_y field matrices are first updated, in that order, using Eqs. (10)–(13). The appropriate time sample of the source pulse function is then fed into the E_y field component at the current source location, and the E_y wavefield is recorded at all of the receiver locations. The output from our codes is a data cube containing a series of common-source gathers (i.e., we record multi-offset data). Extraction of common-offset data, which is typically acquired during reflection GPR profiling, from the multi-offset data cube is a trivial matter in MATLAB.

4. Examples

We now show examples of reflection and cross-hole GPR modeling using the codes `TM_model2d.m` and `TE_model2d.m`, respectively. The programs are called with the example run scripts `TM_run_example.m` and `TE_run_example.m`. Fig. 4 shows the electrical property model used for the TM-mode, reflection GPR example. The subsurface consists of two layers separated by a dipping boundary. The upper layer, representative of vadose zone sediment, has $\epsilon_r = 9$ and $\sigma = 1$ mS/m. The lower layer, representative of material in the saturated zone, has $\epsilon_r = 25$ and $\sigma = 5$ mS/m. Within the upper layer there are three anomalous blocks of different sizes having $\epsilon_r = 16$ and $\sigma = 1$ mS/m. For all materials, μ was set equal to its free space value, μ_0 . An air–earth interface is included in the model at $z = 0$; this was accomplished by simply adding a thin upper layer with $\epsilon_r = 1$ and $\sigma = 0$ to the grid. Sources and receivers were located along the air–earth interface every 0.2 m for the reflection survey. The Blackman–Harris source pulse had a dominant frequency of 100 MHz. For this pulse and

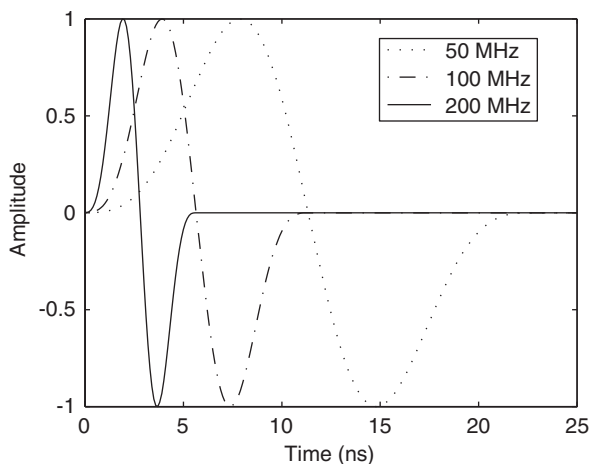


Fig. 2. Examples of Blackman–Harris pulses fed into grid as sources in our FDTD modeling codes.

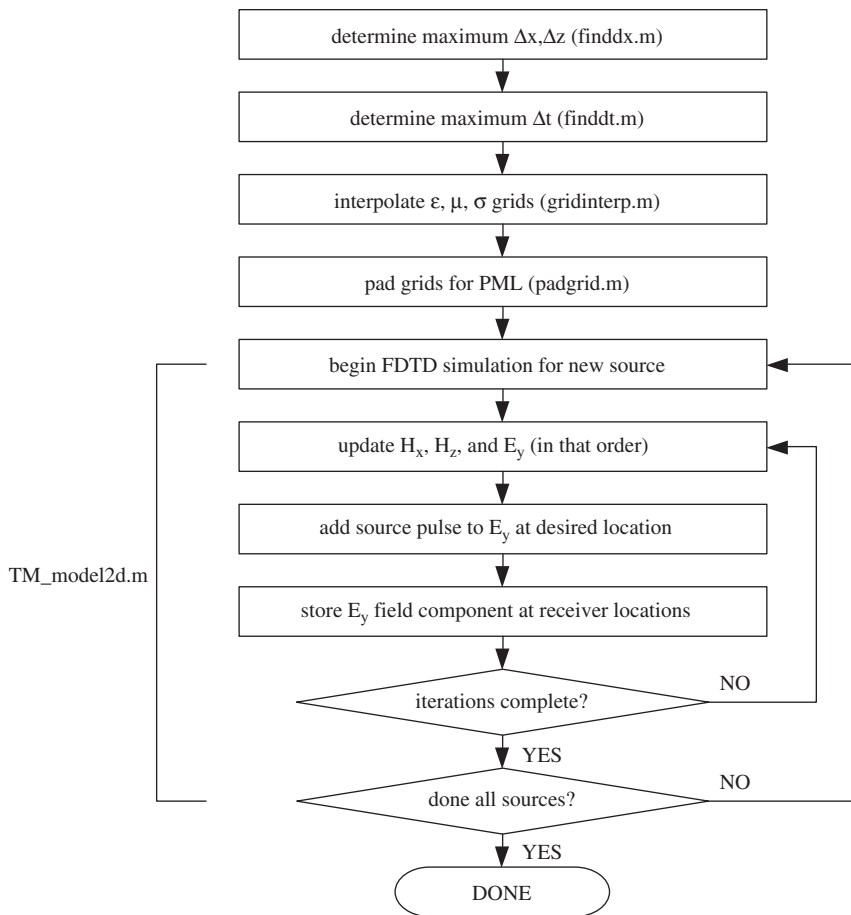


Fig. 3. Flowchart of FDTD modeling procedure.

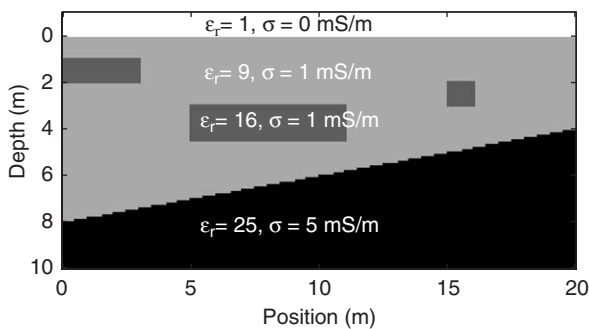


Fig. 4. Electrical property model used for TM-mode reflection GPR example.

the electrical properties in the model, `finddx.m` yielded a maximum possible spatial discretization of 0.0423 m. We used $\Delta x = \Delta z = 0.04$ m. The maximum possible time step, determined using `finddt.m`, was 0.0801 ns. We used $\Delta t = 0.08$ ns.

Fig. 5 shows snapshots of the E_y field component at various times during the FDTD simulation for

the source located at $x = 10$ m. Because of the PML absorbing boundaries implemented in our code, no reflections can be seen coming from the edges of the modeling domain in any of the panels. At $t = 30$ ns, we capture the wavefield as it is spreading outwards from the source before it has encountered any heterogeneities within the earth. Head waves link the energy traveling more rapidly through the air with that traveling through the ground. At $t = 50$ ns, the wavefield has clearly encountered the large anomalous block in the middle of the upper layer, and has been partly reflected back towards the surface. The direct wave traveling through the air from the source location has also left the boundaries of the modeling domain at this point. At $t = 70$ ns, the energy reflected from the block in the upper layer has reached the air–earth interface. At $t = 90$ ns, we see the wavefield being reflected from the dipping boundary between the top and bottom layers. Fig. 5 clearly shows that, even for the relatively simple earth model shown in Fig. 4, the

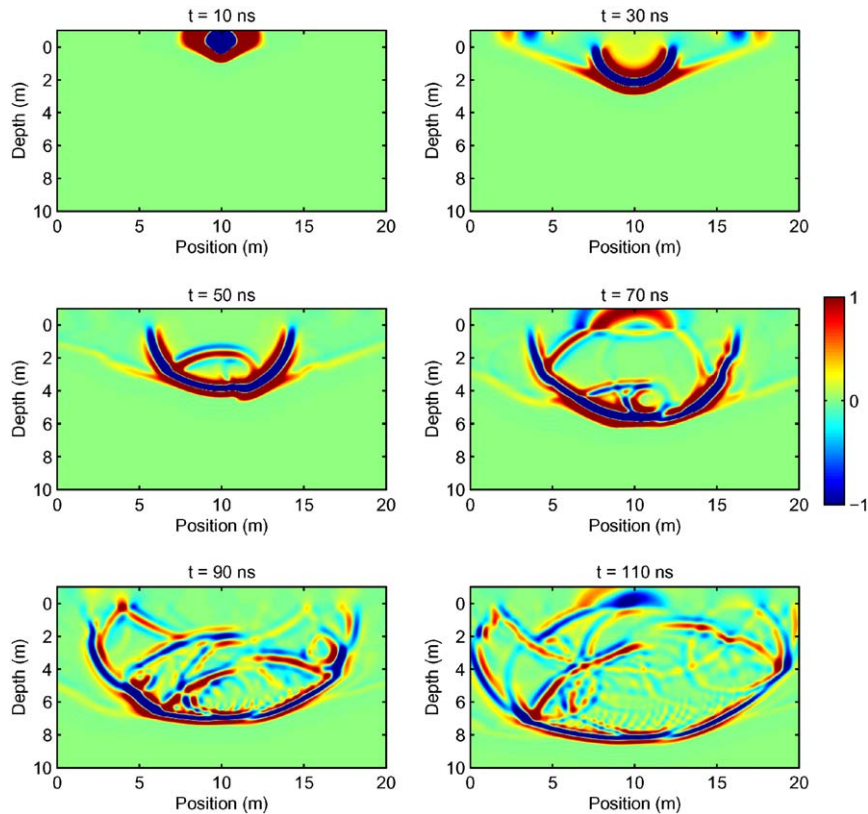


Fig. 5. Snapshots showing amplitude of E_y wavefield at different times during TM-mode FDTD modeling. Source is located at $x = 10$ m, $z = 0$ m.

propagating wavefield becomes quite complicated very quickly.

Fig. 6 shows one of the common-source gathers (consisting of the recorded E_y field component in time at all of the receiver locations) for the source located at $x = 10$ m in Fig. 4. This is one slice of the output multi-offset data cube. The linear events in the image are the direct air and ground arrivals. The events with hyperbolic moveout are reflections from the top and bottom of the block anomaly in the middle of the upper layer, and the dipping boundary between the upper and lower layers. Fig. 7, on the other hand, shows the common-offset reflection GPR data that were extracted from the data cube. The source–receiver offset for this image is 1 m. In the image, diffractions are clearly seen originating from each corner of the block anomalies. Also, the dipping boundary between the upper and lower layers is strongly visible, although it is not a perfectly straight interface in the GPR section because of time shifts caused by the velocity anomalies in the upper layer. Finally, the direct air

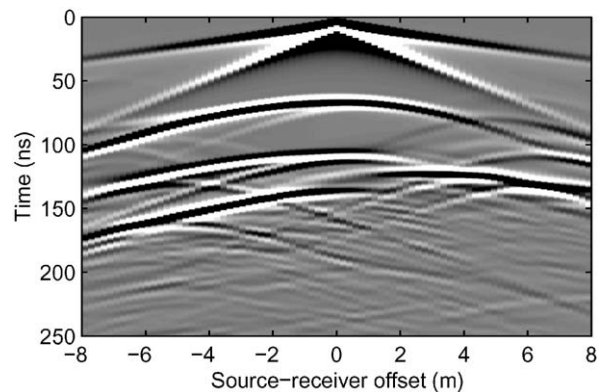


Fig. 6. Common-source gather for source located at $x = 10$ m, $z = 0$ m in Fig. 4.

and ground waves are merged together and present at the top of Fig. 7.

In our second example, we demonstrate FDTD modeling of a crosshole GPR survey using TE_{mode}12d.m. Fig. 8 shows the subsurface EM-wave velocity of the survey plane, which was obtained

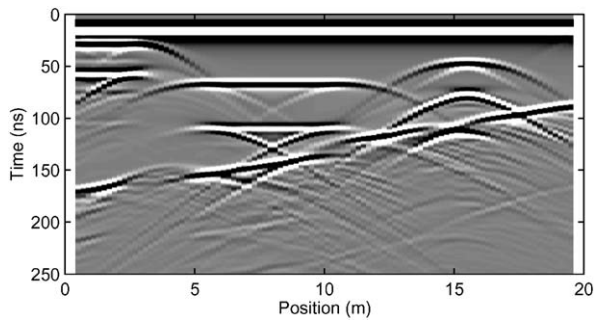


Fig. 7. Common-offset gather for TM-mode reflection GPR modeling example.

from the distribution of relative dielectric permittivity using the following low-loss approximation:

$$v = \frac{c}{\sqrt{\epsilon_r}}, \quad (18)$$

where c is the velocity of EM waves in free space (0.3 m/ns). The permittivity model was constructed using the GSLIB geostatistical software package (Deutsch and Journel, 1992). Relative permittivity values were set to vary between 20 and 32, a range which is typical of materials in the saturated zone. A constant conductivity of 5 mS/m was assumed, and μ was again set equal to its value in free space. Sources were located every 0.25 m from 0.5 to 10.5 m depth down a borehole located at $x = 0.5$ m. Receivers were located at the same depths in a borehole located at $x = 5.5$ m. Again, a Blackman–Harris pulse with a dominant frequency of 100 MHz was used as a source function. For this example, `finddx.m` yielded a maximum spatial discretization interval of 0.0374 m. We used $\Delta x = \Delta z = 0.025$ m. The maximum possible time step determined using `finddt.m` was 0.0226 ns. We used $\Delta t = 0.02$ ns. The air–earth interface was not modeled in this example to facilitate the automatic picking of travel times through the earth in the resulting data.

Fig. 9 shows snapshots of the E_z field component at various times during the crosshole modeling when the E_z source was located at $z = 2$ m. The propagating wavefront in this case is much more circular than that shown in Fig. 5 because the magnitudes of the velocity heterogeneities in this example are quite small. Small variations in velocity were purposely used in this example so that the resulting travel time data could be inverted reasonably accurately using a simple, straight-ray tomo-

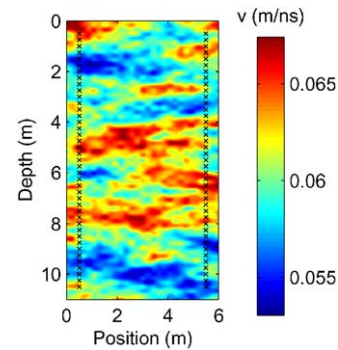


Fig. 8. Subsurface velocity model for TE-mode crosshole GPR example. Source and receiver locations are marked by an 'x'.

graphy code. Despite this, low-amplitude reflections are clearly seen in Fig. 9, which arise from the velocity heterogeneities.

Fig. 10 shows one of the common-source gathers that was obtained in this example for the E_z source located at $z = 5$ m in Fig. 8. The first-arrival times in each common-source gather (i.e., the arrival times for each source–receiver configuration in the survey) were picked automatically from the data based on the first point in each trace where the amplitude exceeded 1% of the trace maximum. These noise-free travel-time data were then inverted using a straight-ray, least-squares, tomography algorithm with a small amount of second derivative smoothness regularization added for stability. Fig. 11 shows the resulting velocity tomogram. Compared with Fig. 8, we see that the inversion of the noise-free travel-time data, as expected, produces a very good image of the subsurface velocity field. There is a small amount of smearing in the image along some of the high-angle raypath directions. Also, the resolution of the inversion result is slightly worse than that of the true velocity model, due to the resolution limits of ray-based tomography, the aperture-limited nature of the survey, and errors resulting from our straight ray approximation.

5. Conclusions

The codes presented here provide a relatively easy-to-understand, flexible package for 2-D GPR modeling in MATLAB. Although the use of MATLAB means that our codes are slightly slower than similar compiled C or Fortran routines, the MATLAB environment offers significant benefits over these other programming languages such as increased code readability and easier plotting and

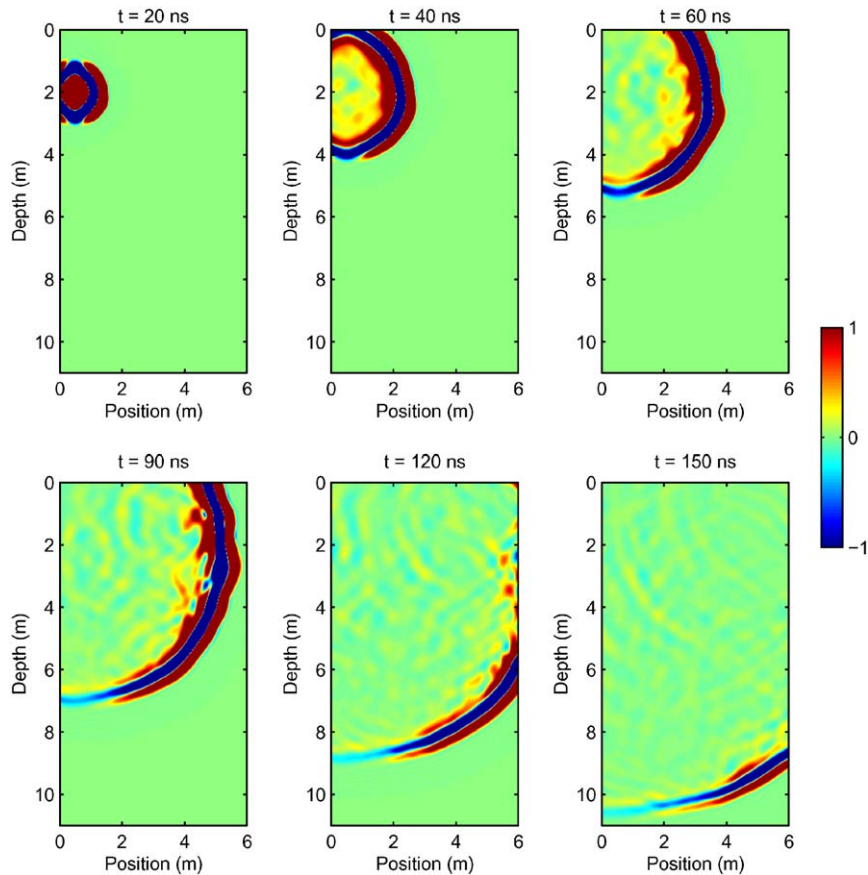


Fig. 9. Snapshots showing amplitude of E_z wavefield at different times during TE-mode FDTD modeling. Source is located at $x = 0.5$ m, $z = 2$ m.

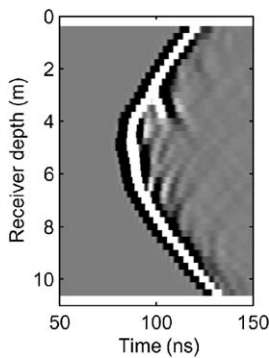


Fig. 10. Common-source gather for source located at $x = 0.5$ m, $z = 5$ m in Fig. 8.

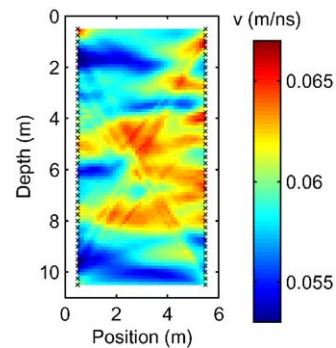


Fig. 11. Straight-ray velocity tomogram obtained from synthetic crosshole data created using our TE-mode code.

manipulation of data. Our codes are well suited to be modified for more complex modeling if desired, an example being to alter them to allow for dispersion in electrical properties. The possibility also exists, for very long reflection GPR surveys, for

the run scripts that we have provided to be modified so that only the subsurface region contributing to the traces being recorded is considered. This could be done without altering the main code, `TM_model2d.m`, and could significantly decrease the modeling time for very long survey lines.

Acknowledgements

This research was supported by funding to R. Knight from the National Science Foundation, Grant Number EAR-0229896-002. J. Irving was also supported during this work through a Departmental Chair's Fellowship at Stanford University.

Appendix A. Supplementary data

Supplementary data associated with this article can be found in the online version, at [10.1016/j.cageo.2005.11.006](http://dx.doi.org/10.1016/j.cageo.2005.11.006).

References

- Berenger, J.P., 1994. A perfectly matched layer for the absorption of electromagnetic waves. *Journal of Computational Physics* 114, 185–200.
- Bergmann, T., Robertsson, J.O.A., Holliger, K., 1996. Numerical properties of staggered finite-difference solutions of Maxwell's equations for ground-penetrating radar modeling. *Geophysical Research Letters* 23, 45–48.
- Bergmann, T., Robertsson, J.O.A., Holliger, K., 1998. Finite-difference modeling of electromagnetic wave propagation in dispersive and attenuating media. *Geophysics* 63, 856–867.
- Bourgeois, J.M., Smith, G.S., 1996. A fully three-dimensional simulation of a ground-penetrating radar: FDTD theory compared with experiment. *IEEE Transactions on Geoscience and Remote Sensing* 34, 36–44.
- Cai, J., McMechan, G.A., 1995. Ray-based synthesis of bistatic ground-penetrating radar profiles. *Geophysics* 60, 87–96.
- Carcione, J.M., 1996. Ground-penetrating radar: wave theory and numerical simulation in lossy anisotropic media. *Geophysics* 61, 1664–1677.
- Casper, D.A., Kung, K.S., 1996. Simulation of ground-penetrating radar waves in a 2-D soil model. *Geophysics* 61, 1034–1049.
- Chen, Y.H., Chew, W.C., 1997. Application of perfectly matched layers to the transient modeling of subsurface EM problems. *Geophysics* 62, 1730–1736.
- Chew, W.C., Weedon, W.H., 1994. A 3-D perfectly matched medium from modified Maxwell's equations with stretched coordinates. *IEEE Microwave and Optical Technology Letters* 7, 599–604.
- Deutsch, C.V., Journel, A.G., 1992. *GSLIB: Geostatistical Software Library and User's Guide*. Oxford University Press, New York, NY, 340pp.
- Ellefsen, K.J., 1999. Effects of layered sediments on the guided wave in crosswell radar data. *Geophysics* 64, 1698–1707.
- Fang, J., Wu, Z., 1996. Generalized perfectly matched layer for the absorption of propagating and evanescent waves in lossless and lossy media. *IEEE Transactions on Microwave Theory and Techniques* 44, 2216–2222.
- Gedney, S., 1998. The perfectly matched layer absorbing medium. In: Taflov, A. (Ed.), *Advances in Computational Electrodynamics: The Finite-Difference Time-Domain Method*. Artech House, Norwood, MA, pp. 263–343.
- Georgakopoulos, S.V., Birtcher, C.R., Balanis, C.A., Renaut, R.A., 2002. Higher-order finite-difference schemes for electromagnetic radiation, scattering, and penetration, Part 1: theory. *IEEE Antennas and Propagation Magazine* 44, 134–142.
- Goodman, D., 1994. Ground-penetrating radar simulation in engineering and archeology. *Geophysics* 59, 224–232.
- Harris, F.J., 1978. On the use of windows for harmonic analysis with the discrete Fourier transform. *Proceedings of the IEEE* 66, 51–83.
- Holliger, K., Bergman, T., 2002. Numerical modeling of borehole georadar data. *Geophysics* 67, 1249–1257.
- Kuzuoglu, M., Mittra, R., 1996. Frequency dependence of the constitutive parameters of causal perfectly matched anisotropic absorbers. *IEEE Microwave and Guided Wave Letters* 6, 447–449.
- Luebbers, R.J., Hunsberger, F., 1992. FDTD for Nth-order dispersive media. *IEEE Transactions on Antennas and Propagation* 40, 1297–1301.
- Lui, Q.H., Fan, G., 1999. Simulations of GPR in dispersive media using a frequency-dependent PSTD algorithm. *IEEE Transactions on Geoscience and Remote Sensing* 37, 2317–2324.
- Moghaddam, M., Yannakakis, E.Y., Chew, W.C., 1991. Modeling of subsurface interface radar. *Journal of Electromagnetic Waves and Applications* 5, 17–39.
- Powers, M.H., Olhoeft, G.R., 1994. Modeling dispersive ground-penetrating radar data. *Proceedings of the 5th International Conference on Ground-Penetrating Radar*, Waterloo, Ontario, pp. 173–183.
- Roden, J., Gedney, S., 2000. Convolution PML (CPML): an efficient FDTD implementation of the CFS-PML for arbitrary media. *IEEE Microwave and Optical Technology Letters* 27, 334–339.
- Taflov, A., 1995. *Computational Electrodynamics: The Finite-Difference Time-Domain Method*. Artech House, Norwood, MA, 599pp.
- Teixeira, F.L., Chew, W.C., Straka, M., Oristaglio, M.L., Wang, T., 1998. Finite-difference time-domain simulation of ground-penetrating radar on dispersive, inhomogeneous, and conductive soils. *IEEE Transactions on Geoscience and Remote Sensing* 36, 1928–1936.
- Wang, T., Tripp, A.C., 1996. FDTD simulation of EM wave propagation in 3-D media. *Geophysics* 61, 110–120.
- Xu, T., McMechan, G.A., 1997. GPR attenuation and its numerical simulation in 2.5 dimensions. *Geophysics* 62, 403–414.
- Yee, K., 1966. Numerical solution of initial boundary value problems involving Maxwell's equations in isotropic media. *IEEE Transactions on Antennas and Propagation* AP-14, 302–307.
- Zeng, X., McMechan, G.A., Cai, J., Chen, H.W., 1995. Comparison of ray and Fourier methods for modeling monostatic ground-penetrating radar profiles. *Geophysics* 60, 1727–1734.